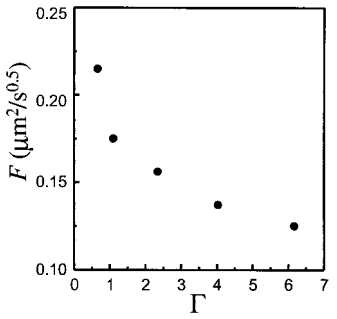

Fig. 4. The single-file particle mobility obtained from the fittings shown in Fig. 2B as a function of the normalized particle interaction strength Γ.

as the conditional probability of finding a particle at position x after time t with the particle located for $t = 0$ at $x = 0$. In Fig. 3A, we show the result of $p(x, t)$ for $\Gamma = 4$ at four different times, which are all greater than t_c. Self-diffusion of particles causes $p(x, t)$ to broaden with time.

Despite the simplicity of the physical situation describing SF conditions, theoretical treatment remains a highly sophisticated task. Analytical results are only obtained for long time limits for hard rods hopping in an infinite 1D lattice (called a 1D exclusion model). It has been predicted that $p(x, t)$ follows (*6, 10, 14*)

$$p(x, t) = \frac{1}{\sqrt{4\pi F t^{1/4}}} \exp(-x^2/4Ft^{1/2}) \quad (2)$$

This form, however, is suggested to remain valid under more general conditions whenever the SF effect is important.

To compare our data with Eq. 2, we replotted the data of Fig. 3A in Fig. 3B; all of the data points collapse to a master curve after a rescaling of the axis. In addition, a Gaussian function fit (Fig. 3B, solid curve) shows good agreement with the data. From the only adjustable parameter of the Gaussian fit, the SF mobility can be derived, which is in agreement with the value obtained from the MSD data. This observation is also true for the $p(x, t)$ for the other magnetic fields. It should be emphasized that Eq. 2 has not been directly observed in experiments before.

The 1D exclusion model predicts that F decreases with the particle density ρ according to $F \propto (1 - \rho)/\rho$. In our system, however, it is more convenient to change the particle interaction strength Γ while keeping the particle density constant. This change is equivalent to changing the particle density because an increase in Γ results in an increase of collision rates between particles or, equivalently, an increase in particle density. The measured mobility (Fig. 4) decreases with the increase of particle interaction energy, which is qualitatively in agreement with the theoretical prediction. However, unlike the hard-rod interaction in the theoretical exclusion model, we have a long-range pair interaction, and the hydrodynamic interactions caused by the particles moving in the surrounding fluid also play an important role. Therefore, detailed comparison with theory should take these two aspects into account.

References and Notes

1. E. J. Harris, *Transport and Accumulation in Biological Systems* (Butterworths Scientific, London, 1960); B. Alberts *et al.*, *Molecular Biology of the Cell* (Garland, New York, 1994).
2. J. Kärger and D. M. Ruthven, *Diffusion in Zeolites and Other Microporous Solids* (Wiley, New York, 1992); N. Y. Chen, T. F. Degnan, C. M. Smith, *Molecular Transport and Reaction in Zeolites* (VCH, New York, 1994).
3. A. L. Hodgkin and R. D. Kenes, *J. Physiol. (London)* **128**, 61 (1955).
4. E. J. A. Lea, *J. Theor. Biol.* **5**, 102 (1963); H. Rickert, *Z. Phys. Chem. Neue. Folge.* **43**, 129 (1964); D. G. Levitt, *Biochim. Biophys. Acta* **373**, 115 (1974).
5. P. A. Rosenberg and A. Finkelstein, *J. Gen. Physiol.* **72**, 341 (1978); S. Draber, R. Schultze, U.-P. Hansen, *J. Membr. Biol.* **123**, 183 (1991); J. A. Hernandez and J. Fischbarg, *J. Gen. Physiol.* **99**, 645 (1992); T. Chou and D. Lohse, *Phys. Rev. Lett.* **82**, 3552 (1999).
6. R. Arratia, *Ann. Probab.* **11**, 362 (1983).
7. P. M. Richards, *Phys. Rev. B* **16**, 1393 (1977); P. A. Fedders, *Phys. Rev. B* **17**, 40 (1978).
8. T. Halpin-Healy and Y. C. Zhang, *Phys. Rep.* **254**, 215 (1995).
9. S. Alexander and P. Pincus, *Phys. Rev. B* **18**, 2011 (1978).
10. H. van Beijeren, K. W. Kehr, R. Kutner, *Phys. Rev. B* **28**, 5711 (1983).
11. J. Kärger, *Phys. Rev. A* **45**, 4173 (1992); *Phys. Rev. E* **47**, 1427 (1993); K. Hahn and J. Kärger, *J. Phys. A Math. Gen.* **28**, 3061 (1995).
12. G. Nägle, *Phys. Rep.* **272**, 215 (1996); X. Qiu, H. D. Ou-Yang, P. M. Chaikin, *J. Phys. (Paris)* **49**, 1043 (1988); A. van Blaaderen, J. Peetermans, G. Maret, J. K. G. Dhont, *J. Chem. Phys.* **96**, 4591 (1992).
13. V. Gupta *et al.*, *Chem. Phys. Lett.* **247**, 596 (1995).
14. V. Kukla *et al.*, *Science* **272**, 702 (1996); K. Hahn, J. Kärger, V. Kukla, *Phys. Rev. Lett.* **76**, 2762 (1996).
15. S. S. Nivarthi, A. V. McCormick, H. T. Davis, *Chem. Phys. Lett.* **229**, 197 (1994).
16. H. Jobic *et al.*, *J. Phys. Chem. B* **101**, 5834 (1997).
17. K. Hahn and J. Kärger, *J. Phys. Chem. B* **102**, 5766 (1998).
18. D. S. Sholl and K. A. Fichthorn, *Phys. Rev. Lett.* **79**, 3569 (1997).
19. R. Radhakrishnan and K. Gubbins, *Phys. Rev. Lett.* **79**, 2847 (1997).
20. K. Zahn, thesis, University of Strasbourg, Strasbourg, France (1997).

21. We thank K. Zahn for giving us the paramagnetic colloidal particles. The work is supported by Deutsche Forschungsgemeinschaft through grant SFB513.

20 September 1999; accepted 8 December 1999

Three-Dimensional Direct Imaging of Structural Relaxation Near the Colloidal Glass Transition

Eric R. Weeks,[1]* J. C. Crocker,[2] Andrew C. Levitt,[2] Andrew Schofield,[3] D. A. Weitz[1]

Confocal microscopy was used to directly observe three-dimensional dynamics of particles in colloidal supercooled fluids and colloidal glasses. The fastest particles moved cooperatively; connected clusters of these mobile particles could be identified; and the cluster size distribution, structure, and dynamics were investigated. The characteristic cluster size grew markedly in the supercooled fluid as the glass transition was approached, in agreement with computer simulations; at the glass transition, however, there was a sudden drop in their size. The clusters of fast-moving particles were largest near the α-relaxation time scale for supercooled colloidal fluids, but were also present, albeit with a markedly different nature, at shorter β-relaxation time scales, in both supercooled fluid and glass colloidal phases.

As a glass-forming liquid is cooled, its viscosity smoothly but rapidly increases by many orders of magnitude (*1–4*). This macroscopic viscosity divergence is related to the divergence of the microscopic structural relaxation time (α-relaxation time). Microscopically, a glass still has liquid-like structure; no structural change has been found which would explain the glass transition (*3–5*). Instead, theories for the glass transition focus on microscopic dynamical mechanisms (*1–4, 6–8*). The underlying concept of many of these theories is the Adam and Gibbs hypothesis (*6*), which states that flow in a supercooled fluid involves cooperative motion of

[1]Department of Physics and Division of Engineering and Applied Sciences, Harvard University, Cambridge, MA 02138, USA. [2]Department of Physics and Astronomy, University of Pennsylvania, Philadelphia, PA 19104, USA. [3]Department of Physics and Astronomy, University of Edinburgh, Edinburgh, Scotland EH9 3JZ, UK.

*To whom correspondence should be addressed. E-mail: weeks@deas.harvard.edu

molecules and that the structural arrest at the glass transition is due to a divergence of the size of cooperating regions. Some support for this hypothesis comes from experiments that found dynamical heterogeneity in the relaxations of supercooled fluids (*9*): at a given time, different regions relax with different rates. The size of these regions has been inferred from indirect evidence (*10*), but their spatial structure remains unknown. Thus, definitive corroboration of these concepts, and indeed a detailed theoretical understanding of the glass transition, has remained elusive.

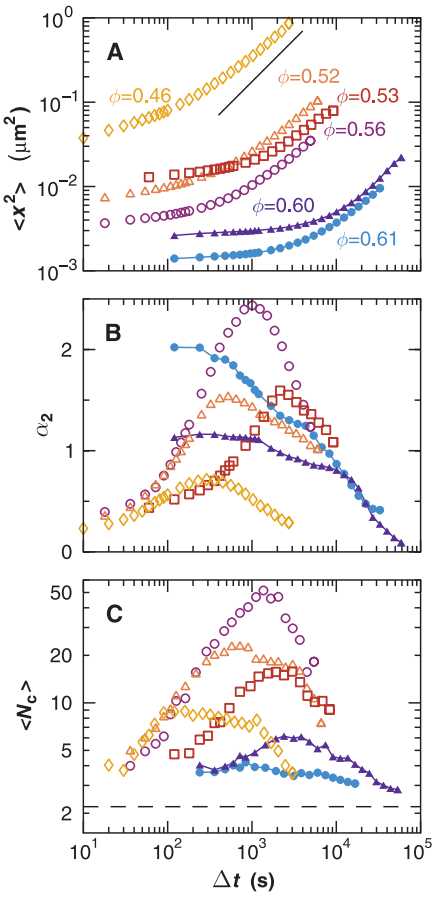

Fig. 1. Relaxation behavior. (**A**) Mean square displacement $\langle \Delta x^2(\Delta t) \rangle$ for several volume fractions ϕ. Open symbols are "supercooled fluids," which form crystals after a few hours (except for ϕ = 0.46, which remains a fluid). Closed symbols are "glasses," which do not form crystals even after several weeks. Although the particles are tracked in three dimensions, only the one-dimensional $\langle \Delta x^2 \rangle$ is shown because the *z* resolution is poorer. The straight line shows a slope of 1. There is inherent uncertainty in these data due to the difficulty in averaging over the temporally and spatially inhomogeneous relaxation processes; see, for example, the data for ϕ = 0.53. (**B**) Nongaussian parameter α_2 calculated from displacements Δx. (**C**) Average cluster size (number of particles) N_c. The dashed line shows the expected result for a random distribution of fast particles (*31*). The symbols for (B) and (C) correspond to the data shown in (A).

Some evidence for cooperative motion in structural relaxation was found very recently in computer simulations of supercooled liquids, which showed that structural relaxation occurred through the motion of relatively few, fast-moving particles (*11–17*). Surprisingly, the positions of the particles were highly correlated and string-like clusters formed, whose size increased as the glass transition was approached (*12*). Unfortunately, however, there has been no direct experimental observation of these three-dimensional (3D) clusters; moreover, it is unlikely that experiments with molecular glasses will directly observe these structures.

Cooperative motion in structural relaxation can, however, be observed in colloidal suspensions, using a microscope to directly image particles (*5, 18–20*). Sterically stabilized colloids are an excellent model of hard spheres (*5, 21–23*), perhaps the simplest system with a glass transition. Although the microscopic, short-time motion of colloidal particles differs from that of model hard spheres because of the suspending fluid, the phase behavior is nevertheless in excellent agreement with predictions for hard spheres (*21, 23*). The thermodynamic variable for hard spheres is the volume fraction ϕ, rather than the temperature. Monodisperse hard spheres form crystals for $\phi \geq 0.494$, with coexistence between crystal and liquid domains for $0.494 \leq \phi \leq 0.545$, and form glasses for $\phi > \phi_G \approx 0.58$ (*21*). The liquid disorder of low volume fraction colloidal suspensions can be quenched into a glass by centrifugation. In a concentrated hard-sphere system, individual particles are trapped in transient cages formed by their neighbors. Structural relaxation is due to the rearrangement of these cages, and the time scale for cage rearrangement, the α-relaxation time, diverges at ϕ_G (*18, 23*). Although this relaxation has been extensively studied with light scattering, direct 3D visualization of these dynamics has not been reported, precluding any detailed study of the structure and dynamics of the relaxing clusters.

We have now used confocal microscopy to follow the motion of several thousand colloidal particles in order to determine directly how motion occurs before and at the α-relaxation time scale. The faster-moving particles move cooperatively in supercooled fluids and form large extended clusters whose size increases dramatically as the glass transition is approached. We have characterized the sizes and structures of these clusters. In addition, at shorter time scales (β-relaxation) the clusters are much smaller, and similar clusters persist even for glassy samples. The use of 3D, time-resolved confocal microscopy is essential for these studies; 2D time-resolved experiments observed some cooperative motion but could not provide any insight into the structure and distribution of clusters (*19, 20*), whereas 3D static images only determined average structure of the glass (*5*).

We used poly-(methylmethacrylate) particles, sterically stabilized by a thin layer of poly-12-hydroxystearic acid (*24*). The particles have a radius a = 1.18 μm, a polydispersity of ~5%, and were dyed with rhodamine and suspended in a cycloheptylbromide/decalin mixture which nearly matches both the density and the index of refraction of the particles. We used a confocal microscope to rapidly acquire images (15 images per second) in a viewing volume of 69 μm × 65 μm × 14 μm; we focused at least 25 μm away from the cover slip to avoid wall effects. We identified particle positions with a horizontal accuracy of 0.03 μm and a vertical accuracy of 0.05 μm, and tracked every particle for the entire duration of the experiment (*25*). We determined ϕ for each sample by measuring the volume per particle directly with the microscope; the ϕ found by this method agrees with the known phase behavior of hard spheres at coexistence. Samples were stirred several hours before observation.

We determined the characteristic relaxation times by calculating the ensemble-averaged mean square displacement (MSD) for different volume fractions, plotted in Fig. 1A. The MSD decreased as the volume fraction increased. The initial plateau in the MSD in Fig. 1A reflects the cage-trapping, and the slow rise is due to the β-relaxation (*8*). The end of this plateau where the MSD rises corresponds to cage rearrangement (*18*) and occurs at larger lag times Δt as the glass transition is approached. For fluid samples (open symbols), the longer time rise in the MSD is due to the α-relaxation. The nature of this motion is illustrated by the particle track shown in Fig. 2; the cage-breaking rearrangement corresponds to rarely occurring large steps in the particle displacement. The long-time diffusion coefficient decreases with increasing volume fraction ϕ and signals the approaching

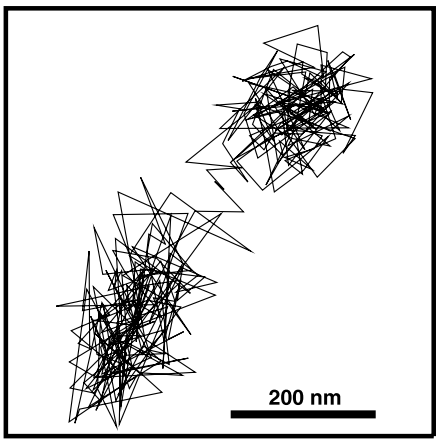

Fig. 2. A typical trajectory for 100 min for ϕ = 0.56. Particles spent most of their time confined in cages formed by their neighbors and moved significant distances only during quick, rare cage rearrangements. The particle shown took ~500 s to shift position. The particle was tracked in 3D; the 2D projection is shown.

glass transition (*8, 26*). To better characterize the α-relaxation, we determined the distribution of particle displacements $P[\Delta x(\Delta t)]$ (Fig. 3). Although this distribution is gaussian for purely diffusive particles, it is expected to be considerably broader near the α-relaxation (*11, 18, 19*). Deviations from a gaussian are quantified by a nongaussian parameter

$$\alpha_2(\Delta t) = \frac{\langle \Delta x^4 \rangle}{3\langle \Delta x^2 \rangle^2} - 1 \qquad (1)$$

the simplest combination of the second and fourth moments of a 1D $P[\Delta x(\Delta t)]$, which is zero for a gaussian distribution (*27*). Broader distributions result in large values of α_2. As in Fig. 1B, for supercooled fluids (open circles), α_2 is largest for lag times corresponding to the end of the cage-trapping plateau in the MSD. We see a clear indication of the approach to the glass transition in the rise of the peak value of α_2 as ϕ increases toward ϕ_G. Note that the magnitude of α_2 may be increased due to the slight polydispersity (5% by radius) of the particles (*17*).

A dramatic change in the behavior of α_2 occurred at $\phi \approx 0.58$; at lower ϕ, α_2 exhibited a distinct peak near the α-relaxation, whereas at higher ϕ, the peak in α_2 was much broader but not as high. We identify this sharp change as the glass transition and determine $\phi_G = 0.58 \pm 0.01$, in agreement with previous work (*18, 21*). For glasses (closed symbols), α_2 drops at longer lag times, even at lag times when the MSD begins to rise (*19*). The upturn in the MSD at longer lag times for the glasses has been seen in other experiments (*18, 19, 28*) and may be due to activated processes (*1*).

To study structural relaxations in supercooled fluid samples, we examined the fastest moving particles: For Δt^* when α_2 is a maximum, the fastest particles are precisely the particles contributing to the tails of $P[\Delta x(\Delta t^*)]$, thus making α_2 large (Fig. 3). We chose a cutoff Δr^* for a given sample such that over time, 5% of the particles had displacements $|\Delta \vec{r}| \geq \Delta r^*$ (*11, 14, 29*), although at any given time, the exact fraction may not be 5%. On average, these particles had moved five times farther than the ensemble of particles ($\Delta r^*/\sqrt{\langle x^2 \rangle} \approx 5$). The 5% most mobile particles were also examined in simulations (*14*), but the cutoffs Δr^* were typically larger than the particle radius a, whereas for our data, Δr^* is typically $0.4a - 0.8a$. The difference may be due to the binary size distribution or to the different particle interaction potential used in the simulations. To look for spatial correlations of these fast particles, we constructed the 3D Delaunay triangulation of the particle positions (*30*), which provides the nearest neighbor connectivity, and we identified the clusters of connected fast particles.

For the supercooled fluid, the fast particles were strongly spatially correlated and exhibited large extended clusters (Fig. 4A). This result is a dramatic demonstration that the α-relaxation in colloidal fluids occurs by means of cooperative particle motion: when one particle moves, another particle moves by closely following the first (*12, 13, 19, 20*). We calculated the angles between displacement vectors of neighboring fast particles; the distribution of these angles is strongly peaked at 0° and shows that neighboring particles move in parallel directions. Moreover, we found that the displacement vectors are more likely to point toward other fast particles than elsewhere, confirming that the motion is cooperative.

We characterized the nature of these clusters by observing the samples in 3D for several hours. The distribution of cluster sizes for a given volume fraction is broad (Fig. 5A); $P(n_c) \sim n_c^{-\mu}$ with $\mu = 2.2 \pm 0.2$ for the supercooled fluids, similar to the value $\mu = 1.9 \pm 0.1$ seen in simulations (*14*). An exponent $\mu < 3$ implies that quantities which depend on $\langle n_c^2 \rangle$, such as average cluster size, will be dominated by the largest clusters; thus, structural relaxation occurs because of a small number of large clusters of cooperative fast particles, rather than many individual fast particles moving independently. It is likely that the distributions of cluster sizes are even broader than indicated because the largest clusters extend out of the viewing volume.

The cluster size increased dramatically as ϕ increased (Fig. 5B) (*31*), consistent with the increased size of the cooperatively rearranging regions of the Adam and Gibbs hypothesis (*6*). Moreover, there is a pronounced drop in the average cluster size at $\phi_G \approx 0.58$ (vertical dashed line in Fig. 5B), which signifies the onset of the colloidal glass transition.

The larger clusters are generally extended structures (Fig. 4); thus, we plot the number of particles in a cluster against the cluster's radius of gyration R_g (Fig. 5C). The power law scaling observed is indicative of fractal structure with a fractal dimension $d_f = 1.9 \pm 0.4$ for all volume fractions, comparable to the preliminary value $d_f \approx 1.75$ seen in the simulations (*14*). We further characterized the structure by measuring the number of neighbors, N_f, of each fast particle. For supercooled fluids, the distribution $P(N_f)$ exhibited a broad peak, with ~10% of the particles having $N_f \geq 7$, indicating dense regions of cooperating particles (*32*). A typical $P(N_f)$ for fluids is shown by the open symbols in Fig. 5D.

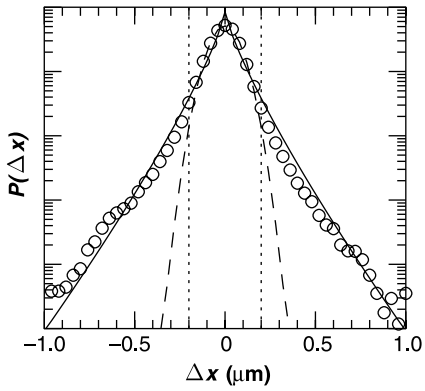

Fig. 3. Distribution function $P(\Delta x)$ for $\phi = 0.56$, at $\Delta t^* = 1000$ s, corresponding to the peak in $\alpha_2(\Delta t)$ (Fig. 1B). The dashed line is the best fit gaussian, and the solid line is a fit of a stretched exponential to the tails of the distribution [$P \sim \exp(-|x/x_0|^\beta)$ with $\beta = 0.8$; we found that $0.8 < \beta < 1.5$ for different choices of ϕ and Δt. Smaller values of β coincide with larger values of α_2]. The data within the dotted lines are the slowest 95%; particles in the fastest 5% have $|\Delta x| > 0.2$ μm.

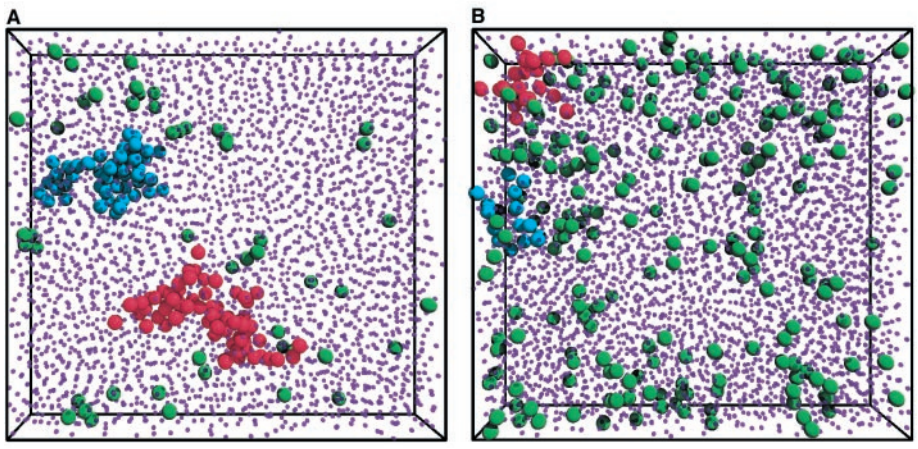

Fig. 4. The locations of the fastest particles (large spheres) and the other particles (smaller spheres). The spheres are drawn smaller for clarity; the particles all have the same physical size, which is the size of the large spheres shown in this figure. (**A**) "Supercooled" sample with $\phi = 0.56$, $\Delta t^* = 1000$ s; the fastest particles had a displacement >0.67 μm. The red cluster contained 69 particles; the light blue cluster contained 50 particles. (**B**) "Glassy" sample with $\phi = 0.61$, $\Delta t^* = 720$ s; the fastest particles had a displacement >0.33 μm. The largest cluster (red) contained 21 particles. The "speed" of a particle was determined over a time Δt^* corresponding to the α-relaxation for (A) and the β-relaxation for (B); see text for details.

What are the dynamical properties of these cooperative clusters? The clusters of fast particles persisted for time scales comparable to Δt^*. Clusters of fast particles appeared in different parts of the sample at different times, so that after many Δt^*, most particles have been "fast" at some time. At all times, clusters of fast particles were present, although at any particular time, the fraction of fast particles in our viewing volume ranged from 2 to 8%. These 3% fluctuations are significantly greater than random fluctuations $\sqrt{N} \approx 0.3\%$. Presumably with a larger viewing volume, the fraction of fast particles at any given time would approach the average value of 5%; the large temporal fluctuations we see are evidence of the large-scale inhomogeneity of fast particles. Further, the presence of these clusters shows that ensemble averaged quantities, such as those shown in Fig. 1 and those obtained in scattering experiments, provide an incomplete picture of the dynamics. For example, $\langle \Delta x^2 \rangle$ increased smoothly (Fig. 1A), whereas the particle motion was in fact temporally and spatially localized (Fig. 4).

The behavior of the clusters of fast particles was markedly different as ϕ_G was crossed. In the supercooled fluid (Fig. 4A), almost all of the fast particles formed a few, very large clusters. In sharp contrast, in the glass (Fig. 4B) there were no large clusters at all, but instead, a large number of smaller clusters. We emphasize however, that the clusters shown for the supercooled fluid correspond to structural (α-) relaxations. In contrast, there was no discernible α-relaxation in our glass data, and instead, the clusters corresponded to the β-relaxation. Indeed, it is not obvious which time scale Δt^* should be used for the glasses, because the average cluster size exhibited only a weak dependence on Δt (Fig. 1C, closed symbols). Moreover, the average cluster size was not correlated with α_2. Thus, for Fig. 4B, we chose Δt^* to correspond to near the middle of the plateau in the MSD ($\Delta t^* \approx 700$ s), clearly reflecting the β-relaxation; however, there was virtually no change in the behavior of the clusters with Δt^*. On all time scales accessible in these experiments, particles remained confined to their cages ($\Delta r^* < 0.4\ \mu\text{m} = a/3$). We found that neighboring particles still moved in similar directions, confirming that the motion was cooperative. In addition, we found no ϕ dependence for the cluster sizes for $\phi > \phi_G$ (Fig. 5B). The distribution of clusters was more narrow, but nevertheless power-law in shape, with the exponent $\mu > 3$ for all glasses (Fig. 5A, closed symbols). The clusters had far fewer compact regions, as indicated by the more narrowly peaked $P(N_f)$ (Fig. 5D, solid symbols).

To properly compare supercooled fluids and glasses, we measured cluster properties for the supercooled fluids at much shorter time scales that correspond to the β-relaxation ($\Delta t = 30$ to 100 s). Their behavior was nearly identical to that of the glass samples, and thus markedly different than the behavior observed at much longer times. The cluster behavior evolved smoothly from β- to α-relaxation over several decades of time for the supercooled fluids. Moreover, the cluster size had nearly the same Δt dependence as the nongaussian parameter α_2 (Fig. 1C, open symbols); this result suggests that at any time scale, the motion of the anomalously fast particles is cooperative. However, only a fraction of the smaller clusters at short time scales ultimately became part of the larger clusters; this evolution was not observed for glasses.

We emphasize that the existence and behavior of the clusters indicates that the relaxations are very inhomogeneous, both temporally and spatially (*9*–*16*). This correlated motion can play a critical role in the dynamics of the sample near the glass transition, and its consequences must be incorporated in any theoretical treatment.

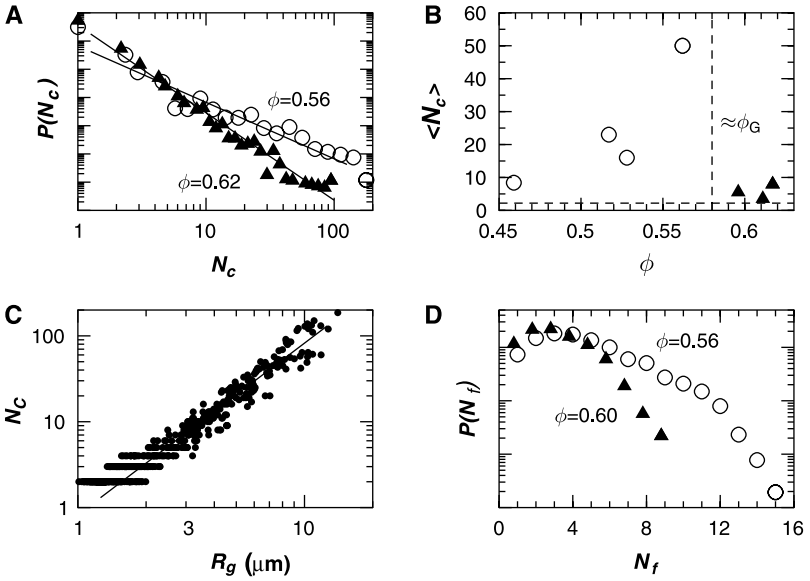

Fig. 5. (**A**) Typical probability distribution functions for cluster sizes (number of particles N_c) for a supercooled fluid ($\phi = 0.56$, open circles) and a glass ($\phi = 0.60$, filled triangles). The lines are least-squares fits to the data, with slopes -2.0 and -3.1, respectively. (**B**) Average size of clusters $\langle N_c \rangle$ at different volume fractions ϕ. The horizontal dashed line indicates the average cluster size that would be expected for a random distribution of fast particles (*31*). For this graph, the clusters for the glasses are defined by choosing the time scale Δt^*, which maximizes the average cluster size. (**C**) Cluster size plotted against the radius of gyration R_g. The power-law behavior indicates fractal scaling, $N \sim R_g^{d_F}$, with a slope $d_F = 2.0$ for the data shown ($\phi = 0.56$, a supercooled fluid). (**D**) Typical distribution functions for N_f, the number of nearest neighbors of a fast particle that are also fast. These functions were computed only for particles within clusters containing at least 15 particles, with the definition of "fast" as the fastest 5%. For randomly distributed fast particles, $N_f \geq 5$ for less than 1% of the fast particles (*31*).

References and Notes

1. C. A. Angell, *J. Phys. Chem. Solids* **49**, 863 (1988).
2. F. H. Stillinger, *Science* **267**, 1935 (1995).
3. M. D. Ediger, C. A. Angell, S. R. Nagel, *J. Phys. Chem.* **100**, 13200 (1996).
4. C. A. Angell, *Science* **267**, 1924 (1995).
5. A. van Blaaderen and P. Wiltzius, *Science* **270**, 1177 (1995).
6. G. Adam and J. H. Gibbs, *J. Chem. Phys.* **43**, 139 (1965).
7. S. A. Kivelson, X. Zhao, D. Kivelson, T. M. Fischer, C. M. Knobler, *J. Chem. Phys.* **101**, 2391 (1994).
8. W. Götze and L. Sjögren, *Rep. Prog. Phys.* **55**, 241 (1992).
9. K. Schmidt-Rohr and H. W. Spiess, *Phys. Rev. Lett.* **66**, 3020 (1991); M. T. Cicerone and M. D. Ediger, *J. Chem. Phys.* **103**, 5684 (1995); R. Böhmer, G. Hinze, G. Diezemann, B. Geil, H. Sillescu, *Europhys. Lett.* **36**, 55 (1996); B. Schiener, R. Böhmer, A. Loidl, R. V. Chamberlin, *Science* **274**, 752 (1996).
10. U. Tracht *et al.*, *Phys. Rev. Lett.* **81**, 2727 (1998).
11. W. Kob, C. Donati, S. J. Plimpton, P. H. Poole, S. C. Glotzer, *Phys. Rev. Lett.* **79**, 2827 (1997).
12. C. Donati *et al.*, *Phys. Rev. Lett.* **80**, 2338 (1998).
13. C. Donati, S. C. Glotzer, P. H. Poole, *Phys. Rev. Lett.* **82**, 5064 (1999).
14. C. Donati, S. C. Glotzer, P. H. Poole, W. Kob, S. J. Plimpton, *Phys. Rev. E* **60**, 3107 (1999).
15. G. Parisi, *J. Phys. Chem. B* **103**, 4128 (1999).
16. R. Yamamoto and A. Onuki, *Phys. Rev. Lett.* **81**, 4915 (1998).
17. B. Doliwa and A. Heuer, *J. Phys. Condens. Matter* **11**, A277 (1999).
18. A. Kasper, E. Bartsch, H. Sillescu, *Langmuir* **14**, 5004 (1998).
19. A. H. Marcus, J. Schofield, S. A. Rice, *Phys. Rev. E* **60**, 5725 (1999).
20. W. K. Kegel and A. van Blaaderen, *Science* **287**, 290 (2000).
21. P. N. Pusey and W. van Megen, *Nature* **320**, 340 (1986).
22. E. Bartsch, V. Frenz, S. Möller, H. Silescu, *Physica A* **201**, 363 (1993).
23. W. van Megen and S. M. Underwood, *Phys. Rev. E* **49**, 4206 (1994).
24. L. Antl *et al.*, *Colloids Surf.* **17**, 67 (1986).
25. J. C. Crocker and D. G. Grier, *J. Colloid Interface Sci.* **179**, 298 (1996).
26. M. Tokuyama and I. Oppenheim, *Phys. Rev. E* **50**, R16 (1994).
27. A. Rahman, *Phys. Rev.* **136**, A405 (1964).
28. W. van Megen, T. C. Mortensen, S. R. Williams, J. Müller, *Phys. Rev. E* **58**, 6073 (1998).

29. In practice, for determining the fastest particles, we considered a new variable $D_i(t_0, \Delta t) = \max_{(t1,t2)} (|\vec{r}_i(t_1) - \vec{r}_i(t_2)|)$, where $t_0 \leq t_1, t_2 \leq t_0 + \Delta t$ and the subscript i is the particle index. This approach is similar to the definition used by previous authors (*12*) and is less sensitive to short-term particle motion. Most results are independent of the cutoff choice Δr^*.
30. F. P. Preparata and M. I. Shamos, *Computational Geometry* (Springer-Verlag, New York, 1985).
31. We computed a particle-averaged cluster size $\langle N_c \rangle \equiv [\Sigma n_c^2 P(n_c)/\Sigma n_c P(n_c)]$ rather than a cluster-averaged size $\Sigma n_c P(n_c)$. The latter measure gave similar results for ϕ and Δt dependence. We computed the expected cluster size for a random distribution of particles by taking the particle speeds at each time t_0, shuffling the particle speeds while keeping the particle positions fixed, and then computing the average cluster size, which is 2.2 ± 0.2 for our data.
32. We found the average particle has 14 nearest neighbors, similar to (*5*).
33. We thank S. C. Glotzer, P. N. Pusey, and P. N. Segrè for useful discussions. Supported by NSF (grants DMR-9631279, DMR-9971432) and NASA (grants NAG3-2058, NAG3-2284).

13 October 1999; accepted 8 December 1999

Oxygen Isotopes and Emerald Trade Routes Since Antiquity

Gaston Giuliani,[1,2]* Marc Chaussidon,[2] Henri-Jean Schubnel,[3] Daniel H. Piat,[4] Claire Rollion-Bard,[2] Christian France-Lanord,[2] Didier Giard,[4] Daniel de Narvaez,[5] Benjamin Rondeau[3]

Oxygen isotopic compositions of historical emerald artifacts from the Gallo-Roman period to the 18th century indicate that during historical times, artisans worked emeralds originating from deposits supposedly discovered in the 20th century. In antiquity, Pakistani and Egyptian emeralds were traded by way of the Silk Route. Together with Austrian stones, they were the only source of gem-quality emeralds. Immediately after the discovery of the Colombian mines by Spaniards in the 16th century, a new trade route was established, first via Spain to Europe and India and then directly via the Philippines to India. Since then, Colombian emeralds have dominated the emerald trade, and most of the high-quality emeralds cut in the 18th century in India originated from Colombia.

Since Egyptian times, emeralds have played a key role in the history of civilizations, being a symbol of eternity and power and an artifact of legend (*1*, *2*). Despite numerous studies based on historical records and on gemological characteristics such as color or mineral and fluid inclusions, the origin of most emeralds set in historical treasures remains uncertain or even enigmatic. This is the case for the so-called "old mine" emeralds (*1*, *3*), which were distributed all over the world by Indian traders under the influence of the Bobur Moghul dynasty in the 16th century. It has been claimed that these famous emeralds came from old mines located somewhere in southeast Asia, although all the deposits in middle and far eastern Asia were officially discovered in the 20th century. Here we describe the results of an oxygen isotopic study of nine emeralds that have acquired an historical dimension and that were selected to cover a large period of time, from the Gallo-Roman epoch to the 18th century. The $^{18}O/^{16}O$ ratio of lattice oxygen in emeralds, added to more classical gemological characteristics, allow us to determine their provenance (*4*) and to document the evolution of emerald trade routes.

The oldest dated artifact we studied is a Gallo-Roman earring (property of the Muséum National d'Histoire Naturelle in Paris) made of gold and emerald and discovered in Miribel (Ain, France) in 1997. We also analyzed four emeralds from the treasury of the Nizam of Hyderabad (India) cut in the 18th century A.D. They are classically called "old mine" emeralds, and their historical record could go back to Alexander the Great (~300 B.C.) (*3*). We also studied the emerald from the Holy Crown of France (51.5 carats, property of the Muséum National d'Histoire Naturelle in Paris), which was set on the central jewel lily of the crown of France by Louis IX (Saint Louis), king of France between 1226 and 1270 A.D. Finally, we studied two large emeralds (property of the Muséum National d'Histoire Naturelle in Paris) that were used by Abbé Hauy, the founder of mineralogy, to describe the mineral emerald in 1806. In addition, we analyzed a rough emerald (1.51 carats, property of the Mel Fisher Maritime Heritage Society in Key West, Florida, USA) that is one of the 2300 stones recovered from the wreck of the *Nuestra Señora de Atocha* Spanish galleon, which sank off the coast of Florida in 1622 A.D. (*5*).

Ion microprobe oxygen isotopic analysis (*6*) shows that these emeralds have variable $\delta^{18}O$ values ranging from 7.5 per mil (‰) to 24.7‰. This range covers nearly all of the range known to exist in emerald deposits worldwide, that is, from 6.2 to 24.8‰ (*4*). It reflects variations in the isotopic composition of the hydrothermal fluids from which emeralds crystallized, the $\delta^{18}O$ value of the fluid being controlled by (i) the composition of the rocks through which the fluids were channeled (*7*), (ii) the intensity of the fluid-rock interactions, and (iii) the temperature of the fluid. Because the $\delta^{18}O$ values in each deposit typically span less than 1‰ (*8*), they are a good fingerprint of the origin of emeralds (Fig. 1). These can be combined with the gemological properties commonly used to characterize emeralds (*9*) in order to determine the origin of emeralds.

Egyptian pharaohs are supposed to have initiated the trade of emeralds by the exploitation of the Cleopatra mines (~1500 B.C.) (*2*). They traded emeralds to Asia, exchanging them for lapis lazuli from Afghanistan. Later, Habachtal emeralds in Austria, known by the Celts, were exploited by the Romans (*1*). Thus, on historical grounds, mines located in Egypt and Austria were the only sources of emerald in the world until 1545 A.D., when the Spaniards exploited the Colombian Chivor mines (*10*). This view is confirmed by the $\delta^{18}O$ value measured for the famous Saint

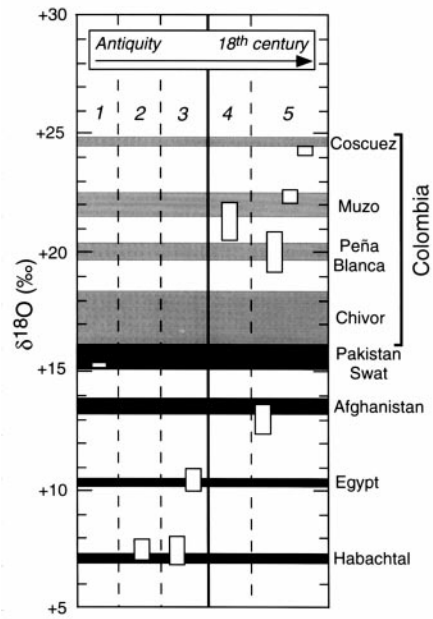

Fig. 1. The $\delta^{18}O$ values of the nine emeralds we analyzed (white boxes). This diagram shows the mining areas (black and gray fields) that are thought to have been exploited historically (*4*). The samples are ordered chronologically. All the samples have $\delta^{18}O$ values that are characteristic of a specific origin. 1: Gallo-Roman earring. 2: Holy Crown of France. 3: Hauy's emeralds. 4: Spanish galleon wreck. 5: old mine emeralds.

[1]Institut de Recherche pour le Développement, [2]Centre de Recherches Pétrographiques et Géochimiques (CRPG)–CNRS, Boite Postale 20, 54501 Vandoeuvre-lès-Nancy, France. [3]Laboratoire de Minéralogie, Muséum National d'Histoire Naturelle, 61 rue Buffon, 75005 Paris, France. [4]Association Française de Gemmologie, 7 rue Cadet, 75009 Paris, France. [5]Compania Mineira Rio Dulce, Carrera 11, Numero 89–38, Oficio 207, Bogotá, Colombia.

*To whom correspondence should be addressed. E-mail: giuliani@crpg.cnrs-nancy.fr